AGU100 ADVANCING EARTH AND SPACE SCIENCE

Geophysical Research Letters

RESEARCH LETTER
10.1029/2020GL087102

A Mechanism for the STEVE Continuum Emission

Brian J. Harding[1], Stephen B. Mende[1], Colin C. Triplett[1], and Yen-Jung Joanne Wu[1]

[1]Space Sciences Laboratory, University of California, Berkeley, CA, USA

Key Points:
- The NO_2 continuum can explain the broadband emission of STEVEs
- N_2 is vibrationally excited via impact by ions inside SAIDs, which enhances NO production and thus the NO_2 continuum
- This process requires 3 eV of translational ion energy, which explains why STEVEs occur only above 130 km and only for the fastest SAIDs

Correspondence to:
B. J. Harding,
bharding@ssl.berkeley.edu

Citation:
Harding, B. J., Mende, S. B., Triplett, C. C., & Wu, Y.-J. J. (2020). A mechanism for the STEVE continuum emission. *Geophysical Research Letters*, *47*, e2020GL087102. https://doi.org/10.1029/2020GL087102

Received 15 JAN 2020
Accepted 13 MAR 2020
Accepted article online 18 MAR 2020

Abstract We describe a mechanism to explain the subauroral emission feature called STEVE (Strong Thermal Emission Velocity Enhancement), with a focus on its continuum spectrum. Spacecraft observations show that emissions co-occur with typically invisible plasma flows known as subauroral ion drifts. If these flows are fast enough, nitrogen molecules are vibrationally excited by collisions with ions, overcoming the activation energy of the $N_2 + O \rightarrow NO + N$ reaction. The resulting NO combines with ambient O, producing NO_2 and spectrally broad light. Importantly, this mechanism also produces N, which reduces the lifetime of NO from hours to seconds and thus explains why the emission is confined to a discrete arc. The predicted emission altitude ($\gtrsim$130 km) and occurrence conditions ($\gtrsim$4-km/s flows) match well with observations. We simulate this mechanism using a simple photochemical model to demonstrate its validity. This mechanism is initiated by fast ion flows and is thus distinct from auroral and airglow processes.

Plain Language Summary Citizen scientists and night-sky photographers have been capturing pictures of a peculiar type of polar light for many years but only recently has the scientific community explored its significance. This narrow purple/white arc stretches east-west across the sky and has come to be known as Strong Thermal Emission Velocity Enhancement (STEVE). Although its appearance is suggestive of aurora, it is not caused by fast electrons from the magnetosphere, and it is dominated by a broad spectrum (mostly white light). Most auroral and airglow emissions are caused by electronic transitions of atmospheric constituents initiated by electron or photon impact, producing spectrally discrete light. The physical processes producing the light in STEVEs are unknown, particularly the chemical mechanism that produces light that could appear white. In this work we describe a candidate mechanism where fast-moving ions cause vibrational excitation of nitrogen molecules, which then undergo chemical reactions to produce spectrally broad light. These fast-moving ions are known to co-occur with STEVEs. This hypothesis is supported by a simple chemical simulation, but observational validation is needed.

1. Introduction

The mechanisms underlying the optical emission known as a Strong Thermal Emission Velocity Enhancement (STEVE) are unknown. The STEVE phenomenon was identified by night-sky photographers and citizen scientists, and it was first reported in the modern scientific literature by MacDonald et al. (2018). STEVEs comprise a thin ribbon of purple light extending east-west for many thousands of kilometers with a north-south width of only a few tens of kilometers (Gallardo-Lacourt et al., 2018). They usually occur about an hour after substorm onset and persists for minutes to hours. A triangulation of citizen scientist photographs found that a STEVE spanned altitudes from 130 to 270 km (Archer, St.-Maurice, et al., 2019). STEVEs are sometimes accompanied by a green "picket fence" structure at lower altitude. In this paper we focus on the mechanisms of the more common purple arc and define "STEVE" to refer to this feature only.

Unlike the aurora, which is energized by particle precipitation from the magnetosphere and comprises discrete spectral lines and bands, STEVEs are mostly broadband (Gillies et al., 2019; Liang et al., 2019) and unrelated to particle precipitation (Gallardo-Lacourt et al., 2018; Nishimura et al., 2019). STEVEs occur equatorward of the boundary of the electron and proton precipitation region (Gallardo-Lacourt et al., 2018; MacDonald et al., 2018; Nishimura et al., 2019). A survey of Swarm satellite overflights confirmed that STEVEs are associated with fast subauroral plasma flows known as subauroral ion drifts (SAIDs) and found a correlation between their occurrence and unusually large plasma velocity, high electron temperature,

and low plasma density (Archer, Gallardo-Lacourt, et al., 2019). Liang et al. (2019) report the altitude of continuum emission at 140–145 km.

These studies have revealed fundamental aeronomical questions. What photochemical mechanism produces the continuum emission in STEVEs? Why is this mechanism only operative above 130 km (i.e., above most of the typical bright airglow and auroral emissions)? What explains the relationship with SAIDs, and why do STEVEs only occur for the strongest SAIDs?

Gillies et al. (2019) discuss known mechanisms producing continuum emission in the upper atmosphere. They consider but ultimately reject emissions arising from meteoric metal compounds such as FeO* and NiO* as the emissions are not broad enough or too weak. Two additional mechanisms mentioned by Gillies et al. (2019) are radiative attachment and NO_2 production:

$$O + e \rightarrow O^- + h\nu \quad (1)$$

$$NO + O \rightarrow NO_2 + h\nu \quad (2)$$

The rate coefficient for radiative attachment is low below 2000 K (Pavlov, 2014). Moreover, inside SAIDs, the electron density is low and the rate is therefore reduced. While it is possible that the rate coefficient is elevated at high temperature, the cross section has been reported up to 2 eV and does not increase significantly with energy (Branscomb, 1962). We thus consider the NO_2 continuum a more likely candidate.

In section 2, we describe a mechanism by which vibrationally excited N_2 enhances production of NO and thus enhances the NO_2 continuum. A time-dependent photochemical model is used to test this hypothesis in section 3. Further discussions and conclusions are given in sections 4 and 5.

2. NO_2 Continuum

The NO_2 continuum emission has been observed from sounding rockets (Enell et al., 2011; Hedin et al., 2012; Mcdade et al., 1986) and orbital platforms (Sheese et al., 2011), and it is thought to explain the vehicle glow observed on the ram surface of the space shuttle (Mende et al., 1988). Its emission rate in the atmosphere is largely controlled by the variable density of NO. Under quiet conditions, the NO_2 continuum is weak, and even in regions of enhanced auroral NO, it only reaches hundreds of Rayleighs (R) in the visible band.

There are three problems with the NO_2 continuum as an explanation for STEVEs:

1. The NO peak density required to explain the observations is roughly 10^{10} cm^{-3}. This is much larger than the largest densities observed even in the auroral zone where production peaks ($1–7 \times 10^8$ cm^{-3}) (Hedin et al., 2012), with the exception of one sounding rocket which measured 10^{10} cm^{-3} (Zipf et al., 1970).
2. Observed NO density profiles peak around 100- to 120-km altitude (Barth, 2010; Stevens et al., 1997; Solomon et al., 1999). STEVEs are observed from 130 to 270 km.
3. The chemical lifetime of NO in the thermosphere is typically hours to days. Because horizontal diffusion and advection timescales are shorter, a thin channel of NO production should create a diffuse and long-lasting glow, not the discrete, transient arc observed.

NO is produced in the thermosphere through various chemical reactions (Barth, 1992; Barth et al., 2009; Grubbs et al., 2018):

$$N + O_2 \rightarrow NO + O \quad (3)$$

$$N(^2D) + O_2 \rightarrow NO + O \quad (4)$$

$$N(^2D) + O_2 \rightarrow NO + O(^1D) \quad (5)$$

$$O^+(^2P) + N_2 \rightarrow NO + N^+ \quad (6)$$

$$O_2^+ + N_2 \rightarrow NO + NO^+ \quad (7)$$

$$N^+ + O_2 \rightarrow NO + O^+ \quad (8)$$

$$N + O \rightarrow NO \quad (9)$$

In each, the reactants include at least one minor species and NO production is thus too slow to produce the required density. Two additional reactions produce NO when N_2 (the dominant constituent below 200 km), is in excited electronic or vibrational states (Campbell et al., 2007):

$$N_2[A^3\Sigma_u^+] + O \rightarrow NO + N(^2D) \quad (10)$$

$$N_2[X^1\Sigma_g^+ \ (v > 11)] + O \rightarrow NO + N \quad (11)$$

where v denotes the vibrational quantum number. Hereafter, we simplify the notation, dropping the ground electronic state: $N_2(v > 11)$.

The former reaction is a source of NO during the day and in regions of auroral precipitation and could be important for STEVEs. However, >6 eV is needed to excite $N_2[A^3\Sigma_u^+]$ and only ~3 eV is needed to excite ground state N_2 to $v > 11$. Ion impact can cause vibrational excitation, and the thermal ion population has been observed to have 3 eV of translational kinetic energy in STEVEs. Thus, we focus here on the latter reaction, which has been previously studied as a significant source of NO (Campbell et al., 2007; Mishin & Telegin, 1989). Ion impact excitation is different than superthermal electron excitation (which is the primary source capable of exciting $N_2[A^3\Sigma_u^+]$), and there is no direct evidence for a superthermal electron population in STEVEs. If a significant population of superthermal electrons is found to exist, the $N_2[A^3\Sigma_u^+]$ pathway should be considered.

The proposed mechanism is shown schematically in Figure 1. In short, a collision with an ion excites N_2 to high vibrational levels. This reacts with O via (11) to produce NO, which then produces white emission via (2). This mechanism is distinct from the aurora, which is caused by particle precipitation, and from airglow, which is caused directly or indirectly by solar radiation.

The proposed mechanism requires a minimum of ~3 eV, equivalent to 4.4 km/s for NO^+, the dominant ion in SAIDs (Anderson et al., 1991). Although not a strict cutoff due to the spread caused by large ion temperatures, this mechanism explains why STEVEs are observed only for the fastest SAIDs. Coincident observations of STEVEs and fast ion flows have been reported for ion velocities of 3.9, 4.8 (Archer, Gallardo-Lacourt, et al., 2019, Figures 1b and 1c), and 5.5 km/s (MacDonald et al., 2018). Typical SAIDs exhibit slower velocities (median 1.3 km/s), and measurements of SAIDs coincident with STEVEs have ion velocities in the top 5% (Archer, Gallardo-Lacourt, et al., 2019).

This mechanism also explains why STEVEs are observed only above 130 km, while most of the bright aurora and chemically sourced airglow occurs at lower altitudes. Below ~130 km, the ion-neutral collision frequency exceeds the ion gyrofrequency (Heelis, 2004), and ions cannot reach the $E \times B$ velocity observed by satellite overflights. Above 130 km, ions can achieve the required kinetic energy.

Finally, the lifetime of NO in this mechanism is reduced from hours to seconds by the simultaneous production of N. The principal loss process for NO is the reaction with N, and vice versa (Barth et al., 2009):

$$NO + N \rightarrow N_2 + O. \quad (12)$$

Equating production and loss for NO and N (reactions (11) and (12)) and using the resulting NO density in reaction (2) yields the expected volume emission rate (VER):

$$\mathrm{VER} = k_2 \left(\frac{k_{11}}{k_{12}} \left[N_2(v > 11) \right] [O]^3 \right)^{\frac{1}{2}} \quad (13)$$

where k_2, k_{11}, and k_{12} are the rate coefficients for reactions (2), (11), and (12), respectively.

An approximate evaluation of this formula follows. We use published rate coefficients (Aladjev & Kirillov, 1995; Barth et al., 2009; Hedin et al., 2012) and expected densities at 150 km for SAID-like conditions, namely, $[O] = 2 \times 10^{10}$ cm^{-3}. Densities of O and N_2 are from the Naval Research Laboratory's Mass Spectrometer and Incoherent Scatter radar Extended 2000 (NRLMSISE-00) (Picone et al., 2002), increased by a factor of ~2

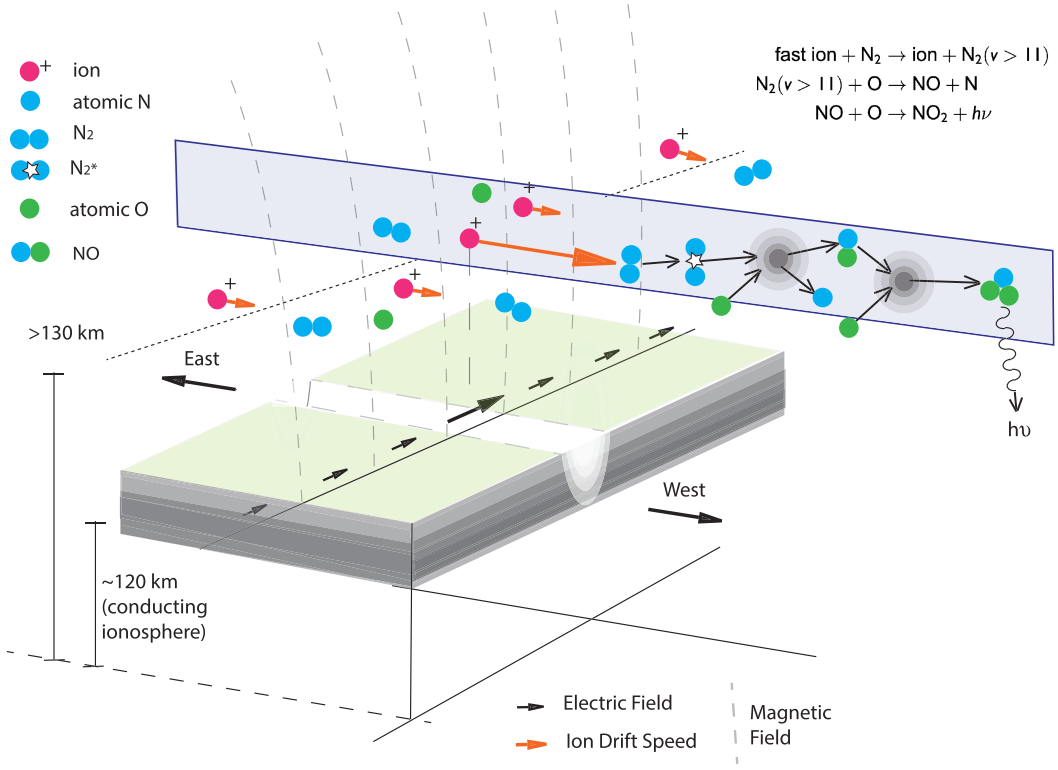

Figure 1. A schematic representation of the proposed mechanism to produce continuum emission inside subauroral ion drifts (SAIDs). A channel of reduced density is shown in the ionosphere. Electric fields across this channel are enhanced, leading to increased ion velocities. Ambient nitrogen molecules are vibrationally excited via impact with these supersonic ions. If excitation reaches $v > 11$ (i.e., vibrational energy equivalent to a 4.4 km/s NO^+ ion), these molecules will react with ambient O to produce NO and N. The NO combines with O to produce NO_2 and continuum emission. Combined with a small amount of OI 630.0-nm emission (not shown here), this yields the characteristic purple color of STEVEs.

to account for the increased temperature (described in more detail in section 3). If ion impact excites 5% of the ambient N_2 to high vibrational energy states, then $[N_2(v > 11)] = 3 \times 10^9$ cm^{-3}. This yields equilibrium densities of $[NO] = [N] = 2.4 \times 10^9$ cm^{-3} and continuum emission of 0.5 $\frac{\text{ph}}{\text{nm cm}^3\text{s}}$. Viewed through an assumed 50-km emission layer and over the 400- to 800-nm wavelength band, this would produce a column brightness of 1,000 *R*.

A $N_2(v > 11)$ fraction of 5% is needed to achieve 1,000 *R* brightness in this calculation. We note that a *v*-dependent value for k_{11} has been calculated by Pavlov (2011) and at $v = 20$ is 10 times larger than the conservative value used here, which is from Aladjev and Kirillov (1995). Thus, the above calculation is also valid for a case where 0.5% of N_2 is excited to $v = 20$. The resulting brightness depends strongly on the vibrational distribution of N_2, which is not well known under these conditions. The excitation of $N_2(v > 11)$ is discussed further in section 4. The resulting brightness also depends strongly on the amount of neutral heating and upwelling via the $[O]^{\frac{3}{2}}$ term. The chemical lifetime of NO in this case is $\left(k_{12}[N]\right)^{-1} = 3$ s, far shorter than the typical lifetime of hours to days. This provides consistency with observations of a thin, discrete arc.

3. Model Results

To support the approximate calculation in the previous section, here a more comprehensive calculation is performed using a time-dependent photochemical model which tracks 15 chemical species and 60 reactions. The following species are explicitly modeled: N, $N(^2D)$, N^+, N_2, $N_2(v > 11)$, N_2^+, NO, NO^+, O, $O(^1D)$, $O(^1S)$, O^+, O_2, O_2^+, and *e*. Rate coefficients are provided in Table A1. Neglected processes include solar and auroral excitation and three-body reactions, which limits the domain to the nighttime thermosphere above ~110-km altitude. Number densities are initialized using NRLMSISE-00 (Picone et al., 2002) and the International

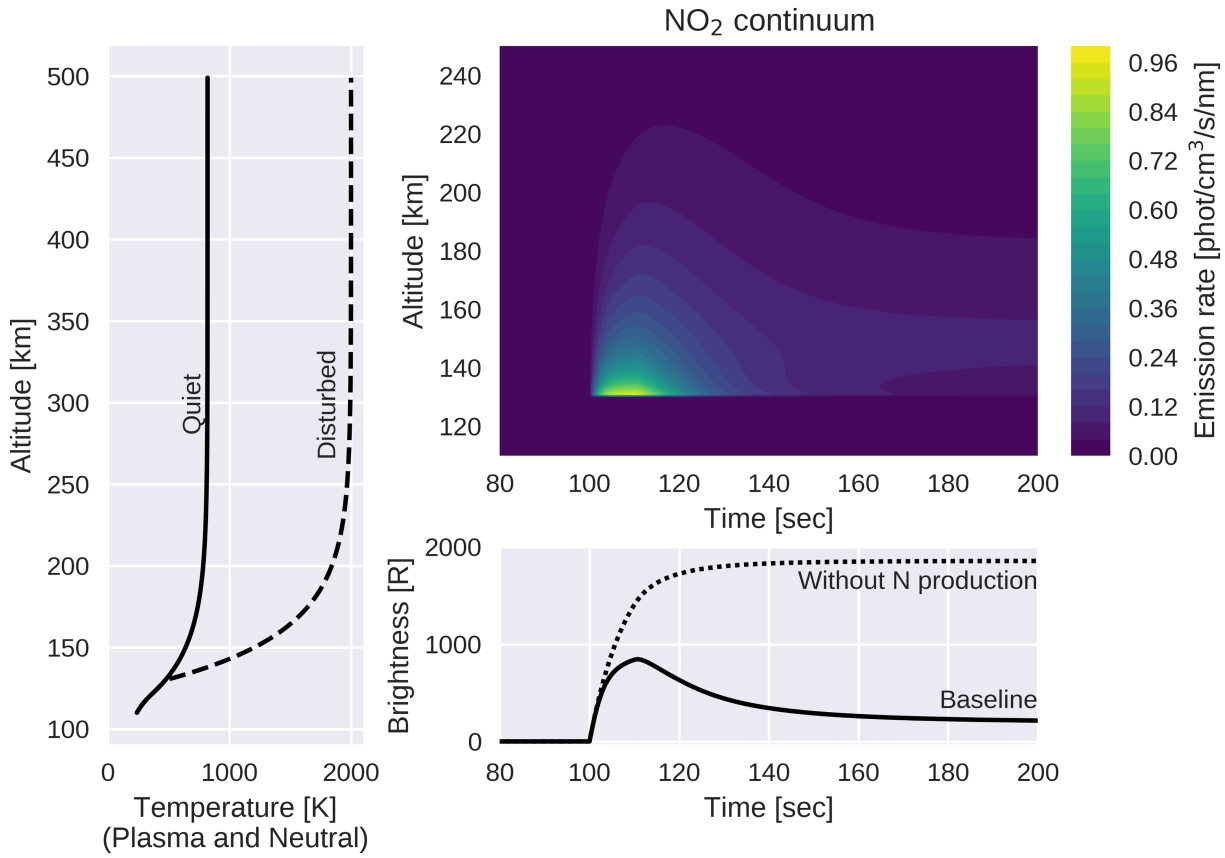

Figure 2. (left) Temperature profiles used in the photochemical model, before (quiet) and after (disturbed) $t = 100$ s. (right, top) Simulated volume emission rate of the NO_2 continuum. (right, bottom) Vertical column brightness of the NO_2 continuum, assuming a 400-nm-wide band. A second diagnostic case is shown, where NO production is initiated without simultaneous production of N.

Reference Ionosphere (Bilitza et al., 2017) models for the time, location, and geophysical conditions of the Gillies et al. (2019) observations. For species not included in these models, densities are initialized assuming chemical equilibrium. The density of $N_2(v > 11)$ is initially set to 0. Although the continuum emission from NO_2 production is included in the model, the density of NO_2 is not, as a newly formed NO_2 molecule is rapidly recycled back to NO and O (Kaufman, 1973).

Starting at $t = 0$ s, a quiet time ionosphere/thermosphere is simulated. At $t = 100$ s, a SAID is imposed, consisting of increased temperature above 130 km. The quiet and disturbed temperature profiles are shown in the left panel of Figure 2. The quiet exospheric temperature is 800 K, while the disturbed case is 2000 K. For simplicity, the plasma and neutral temperatures are set equal. Of course, ion and electron temperatures reach several thousand kelvins and even above 10000 K in SAIDs (Anderson et al., 1991; Archer, Gallardo-Lacourt, et al., 2019). To our knowledge, the neutral temperature inside SAIDs has not been measured, but Khalipov et al. (2018) reported a 500-K neutral temperature increase associated with a 2-km/s subauroral polarization stream. The ion density in this event was likely larger than the ion density inside SAIDs, but the plasma flows that create STEVEs are much faster, and heating is proportional to the square of the ion-neutral relative velocity. The density profiles for major neutral species (O, N_2, and O_2) are adjusted to maintain hydrostatic equilibrium at all times above 130 km.

Also at $t = 100$ s, the $N_2(v > 11)$ fraction is set to 5% above 130 km and this fraction is maintained for 10 s. At $t = 110$ s the model is returned to a free-running state and the $N_2(v > 11)$ population rapidly decays via reaction (11), which turns off the production of NO and N. The NO is destroyed almost entirely via reaction (12) and the continuum brightness diminishes. Altitudes from 110 to 500 km are modeled even though SAID ion velocities are insufficient to produce $N_2(v > 11)$ below 130 km.

Results are shown in the right panels of Figure 2. The top panel shows the modeled emission profile as a function of time and altitude. The bottom panel shows the vertical column brightness integrated over

altitude and over a 400-nm wavelength interval. The emission brightens quickly as soon as the simulated SAID is initiated, reaching 850 *R*. When the N_2 vibrational population is allowed to decay, the emission dims quickly.

For comparison, we also show in the bottom panel a diagnostic model run in which NO production is initiated without simultaneous production of N. In this case the emission remains bright due to the long chemical lifetime of NO. This shows that the production of N is needed to explain the short observed emission lifetime associated with the narrow channel of the emission. However, even with N production, the emission never decays to 0 because although NO and N are initially produced in equal numbers, reaction (3) (an important source of NO under quiet conditions) converts some of the N to NO.

In other numerical experiments (not shown), we find that the brightness is sensitive to certain parameters, which are not well constrained by observations, such as the the altitude profile of Joule heating and neutral upwelling, the rate of reaction (12) at high temperature, the amount of $N_2(v > 11)$, and the vibrational distribution of N_2, among others. For example, if we use $k_{11} = 10^{-10}$ (appropriate for $v = 20$ and $T_n = 2000$ K according to Pavlov, 2011), then the maximum brightness is 2,000 *R*, and it decays to 300 *R*.

4. Discussion

The previous analysis showed that if 5% of the ambient N_2 above 130 km is in high vibrational states and the neutral density is elevated, significant continuum emission is produced. In reality, the amount of vibrationally excited N_2 is not known, and the N_2 vibrational distribution is likely more complex than the simple representation used here. Under a Boltzmann distribution, a vibrational temperature of ~10,000 K is needed to create a $v > 11$ fraction of 5%. However, an equilibrium distribution is not expected. At 150-km altitude, Pavlov, (2011, Figure 1d) calculates the characteristic time for vibrational-vibrational exchange as 160 s. The characteristic time in the model for the $N_2(v > 11)+O$ reaction is $\left(k_{11}[O]\right)^{-1} = 8$ s. This implies that a newly excited $N_2(v > 11)$ molecule will rapidly produce NO before vibrational relaxation takes effect. Certain production and loss processes for lower vibrational states have been neglected here but could be important: high-temperature electron impact, quenching of $O(^1D)$, reaction (12), and vibrational-translational exchange. Accurate kinetic modeling of the vibrational distribution of N_2 is needed.

Regarding vibrational excitation by ion impact, a simple calculation yields an excitation rate that is slower than the instantaneous excitation used in the model. The buildup time to reach a $v > 11$ fraction of 5% is as follows:

$$\tau_{N_2} = \frac{0.05}{\sigma n_i v}, \tag{14}$$

where σ is the ion-neutral impact cross section, n_i is the ion density, and v is the ion-neutral relative velocity. For the purposes of this simple calculation we have made the optimistic assumptions that the neutral atmosphere is dominated by N_2, and ions transfer all of their kinetic energy into N_2 vibrational energy. Using the hard-sphere cross section for NO^+ impact on N_2 ($\sigma = 3.6 \times 10^{-15}$ cm^2), a velocity of 6 km/s, and the ion densities in the model, the buildup time is 350 s at 300 km and 3,000 s at 200 km. These are likely too slow. A better understanding of energetic ion-neutral collisions, vibrational excitation, and the altitude profile of plasma density and velocity is needed for further theoretical development. Missing from this analysis, but potentially important, is the vibrational distribution of ionospheric ions, which is not well understood (Sheehan & St.-Maurice, 2004), and the vibrational distribution of N_2.

In addition to the vibrational distribution, the bulk thermospheric/ionospheric response inside SAIDs is much more complicated than what is represented by this simple model. For example, significant effects of plasma dynamics and heating have been observed (Anderson et al., 1991; Rodger et al., 1992). The amount of neutral upwelling changes the continuum brightness considerably. Additionally, horizontal transport has been shown to be important for modeling subauroral polarization stream/SAID plasma densities (Richards et al., 2014).

This paper focuses on the STEVE continuum emission, which comprises about 95% of its radiance, but the 630.0-nm red line component is of potential interest. The red line emission can be produced by a variety of processes (Solomon et al., 1988). Excitation by collisions with thermal electrons is thought to be the source of stable auroral red (SAR) arcs (Mendillo et al., 2016). Although similarly located in the subauroral region,

STEVEs and SAR arcs are distinct phenomena, as noted by Archer, Gallardo-Lacourt, et al. (2019). SAR arcs occur during the recovery phase of geomagnetic storms and represent the slow decay of ring current energy transmitted down the field line by heat conduction. The electrons in the high-energy tail of the thermal distribution have enough energy to directly excite ambient oxygen atoms to the ^{1}D state, but not enough energy to excite any other significant species. This yields pure red emission around 400-km altitude (Kozyra et al., 1997). STEVEs are distinguished by their narrow latitudinal width, transient appearance, lower altitude, and the presence of other emissions.

Red line enhancements inside SAIDs have been previously studied (Sazykin et al., 2002) and may be related to the phenomenon known as "weak SAR arcs" (Khalipov et al., 2001, 2018; Foster et al., 1994). In this mechanism, a large ion-neutral relative velocity leads to an enhanced O_2^+ and NO^+ recombination rate and thus elevated $O(^1D)$ production. Higher electron temperatures can also play a role, as in classical SAR arcs. It has not been established whether the red enhancements seen in STEVEs are related to this phenomenon nor is it clear whether the red enhancements within STEVEs have been routinely observed (but categorized as a weak SAR arc) by the widespread network of instruments sensitive only to a narrow band of the spectrum at 630.0 nm. In our model (as in Sazykin et al., 2002), dissociative recombination of O_2^+ and NO^+ contribute to red line enhancements in SAIDs. However, because of the large N density, the dominant source of red line in the model is the reaction:

$$O_2^+ + N \rightarrow NO^+ + O(^1D). \tag{15}$$

The red line reaches ~40 *R* in the model, but a quantitatively accurate result will require self-consistent plasma dynamics and heating. If the elevated electron temperatures that have been measured on the topside are any indication of electron temperatures at lower altitudes, accurate knowledge of the profiles of electron density, electron temperature, and oxygen density is needed to evaluate the contribution from thermal electron excitation.

Although this paper is not focused on the green "picket fence" structures, which are sometimes associated with STEVEs, a few remarks are pertinent. The picket fence consists mostly of the 557.7-nm green line (Gillies et al., 2019) and it spans 95–150 km (Archer, St.-Maurice, et al., 2019). While it is well accepted that the purple arc is not caused by particle precipitation, the relation of the picket fence to precipitation is controversial. A picket fence was observed at a location magnetically conjugate to a Defense Meteorological Satellite Program observation of detached precipitation and far ultraviolet aurora (Nishimura et al., 2019). However, precipitation should create N_2^+ first negative emissions, while there is no evidence for this emission in the picket fence spectrum observed by Gillies et al. (2019) (Mende et al., 2019). The horizontal structuring (~18-km spacing) and magnetic field-aligned structure of the picket fence(Archer, St.-Maurice, et al., 2019) are suggestive of precipitation and stand in contrast to the purple arc, which appears much less structured. However, under the proposed mechanism, any underlying structure of the purple arc would be blurred by the lifetime of NO. The radiative lifetime of the green line upper state is 0.8 s. For a 250-m/s horizontal flow (Archer, St.-Maurice, et al., 2019), this gives a blurring width of 0.2 km, which is negligible for the picket fence. However, for the purple arc, the lifetime of the proposed emission mechanism is dominated by the lifetime of NO. In the model, in regions of large NO_2 continuum emission (defined as greater than 50% of the maximum), the lifetime is 3.5–7.7 s. With an assumed velocity of 5 km/s at the NO_2 continuum dominant altitude, the horizontal blurring is 17–39 km, which is of the same order or larger than the horizontal structure. This means it is possible for the green picket fence and purple arc to have the same underlying ~18-km structure even though the purple arc appears more (or completely) diffuse.

5. Conclusion

We have described a mechanism to explain the continuum emission in STEVEs. Nitrogen molecules, excited to high vibrational energy by collisions with supersonic ions, overcome the activation energy of the $N_2 + O \rightarrow NO + N$ reaction. The resulting NO combines with ambient O to produce NO_2 and white light. As this mechanism is only operative where the ions move at the $E \times B$ velocity, it explains why STEVEs are observed above 130 km. It also explains why STEVEs are only observed for high-velocity SAIDs, as 3 eV (equivalent to a 4.4 km/s NO^+ ion or a 6.0 km/s O^+ ion) is needed to excite N_2 to $v > 11$ and thus cause reaction (11). The apparent discrepancy between the thin transient arc and the typically long chemical lifetime of NO is resolved by the simultaneous production of N, which reduces the lifetime to seconds.

Vibrationally enhanced nitrogen was introduced into a photochemical model, resulting in visible levels of continuum emission. Although the computational results lend support to the proposed mechanism, observational validation is needed. More measurements of the spectral shape may help identify or exclude NO_2 as the emitting species. In situ or remote observations of enhanced NO and/or O would be challenging but most direct. However, these would not directly implicate vibrational N_2, which is difficult to observe. Coincident observations of enhanced N would be indirect validation.

Appendix A: Reaction Rates

In Table A1 we list the reactions used in the photochemical model. The reaction rate coefficients were adopted from the compilation of Grubbs et al. (2018), except where noted. The 630.0-nm emission here refers to the combined 630.0- and 636.4-nm lines. If an electronic state is not given, the ground state is implied. All temperatures are in units of kelvin. T_n, T_i, and T_e refer to the neutral, ion, and electron temperature. T_f is the effective ion temperature (St.-Maurice & Laneville, 1998). The variable τ denotes a scaled temperature:

$$\tau = \frac{T}{300} \tag{A1}$$

Table A1
Reaction Rate Coefficients, From Grubbs et al. (2018) Unless Otherwise Noted

Reaction	Rate coefficient (cm^3/s)	Reference
$N_2^+ + O \rightarrow NO^+ + N(^2D)$	$1.4 \times 10^{-10}(1 - 0.07\tau_i^{0.21})\tau_i^{-0.44}$	
	$[T_i < 1,500]$	
	$5.2 \times 10^{-11}(1 - 0.07\tau_i^{0.21})\tau_i^{0.2}$	
	$[T_i \geq 1,500]$	
$N_2^+ + O \rightarrow O^+ + N_2$	$1.4 \times 10^{-10} 0.07\tau_i^{-0.23}$	
	$[T_i < 1,500]$	
	$5.2 \times 10^{-11} 0.07\tau_i^{0.41}$	
	$[T_i \geq 1,500]$	
$N_2^+ + O_2 \rightarrow N_2 + O_2^+$	$5.0 \times 10^{-11}\tau_i^{-0.8}$	
$N_2^+ + e \rightarrow N(^2D) + N$	$1.94 \times 10^{-7}\tau_e^{-0.39}$ $[T_e < 1,200]$	
	$1.72 \times 10^{-7}\tau_e^{-0.57}$ $[T_e \geq 1,200]$	
$N_2^+ + e \rightarrow N(^2D) + N(^2D)$	$2.64 \times 10^{-8}\tau_e^{-0.39}$ $[T_e < 1,200]$	
	$2.34 \times 10^{-8}\tau_e^{-0.57}$ $[T_e \geq 1,200]$	
$O^+ + N_2 \rightarrow NO^+ + N$	1.71676×10^{-12}	
	$-7.19934 \times 10^{-13}\tau_f$	
	$+1.33276 \times 10^{-13}\tau_f^2$	
	$-9.28213 \times 10^{-15}\tau_f^3$	
	$+6.39557 \times 10^{-16}\tau_f^4$	
	$[T_f < 3725]$	
	-1.52489×10^{-11}	
	$+7.67112 \times 10^{-13}\tau_f$	
	$+1.19064 \times 10^{-13}\tau_f^2$	
	$-1.30858 \times 10^{-15}\tau_f^3$	
	$+4.67756 \times 10^{-18}\tau_f^4$	
	$[T_f \geq 3725]$	St.-Maurice and Laneville (1998)
$O^+ + O_2 \rightarrow O_2^+ + O$	2.78932×10^{-11}	
	$-6.92612 \times 10^{-12}\tau_f$	
	$+8.67684 \times 10^{-13}\tau_f^2$	

Table A1
Continued

Reaction	Rate Coefficient [$cm^3\ s^{-1}$]	Reference
	$-3.47251 \times 10^{-14}\tau_f^3$	
	$+5.07097 \times 10^{-16}\tau_f^4$	
	$[T_f < 4800]$	
	-1.74046×10^{-11}	
	$+3.02328 \times 10^{-12}\tau_f$	
	$-2.39214 \times 10^{-15}\tau_f^2$	
	$-4.02394 \times 10^{-17}\tau_f^3$	
	$[T_f \geq 4800]$	St.-Maurice and Laneville (1998)
$O^+ + NO \rightarrow NO^+ + O$	6.40408×10^{-13}	
	$-1.33888 \times 10^{-13}\tau_f$	
	$+7.65103 \times 10^{-14}\tau_f^2$	
	$-3.11509 \times 10^{-15}\tau_f^3$	
	$+6.62374 \times 10^{-17}\tau_f^4$	
	$[T_f < 3800]$	
	-7.48312×10^{-13}	
	$+2.31502 \times 10^{-13}\tau_f$	
	$+3.0716 \times 10^{-14}\tau_f^2$	
	$-2.65436 \times 10^{-16}\tau_f^3$	
	$+7.76665 \times 10^{-19}\tau_f^4$	
	$[T_f \geq 3800]$	St.-Maurice and Laneville (1998)
$O_2^+ + NO \rightarrow NO^+ + O_2$	4.1×10^{-10}	
$O_2^+ + N_2 \rightarrow NO^+ + NO$	5×10^{-16}	
$N_2^+ + NO \rightarrow NO^+ + N_2$	$7.5 \times 10^{-9}\ T_n^{-0.52}$	
$O_2^+ + N \rightarrow NO^+ + O(^1S)$	2.48×10^{-11}	
$O_2^+ + N \rightarrow NO^+ + O(^1D)$	1.40×10^{-10}	
$O_2^+ + e \rightarrow O(^1D) + O$	$1.19 \times 10^{-7}\tau_e^{-0.7}$	
	$[T_e < 1200]$	
	$1.18 \times 10^{-7}\tau_e^{-0.61}$	
	$[T_e \geq 1,200]$	
$O_2^+ + e \rightarrow O(^1D) + O(^1D)$	$7.59 \times 10^{-8}\tau_e^{-0.7}$	
	$[T_e < 1,200]$	
	$7.51 \times 10^{-8}\tau_e^{-0.61}$	
	$[T_e \geq 1,200]$	
$O_2^+ + e \rightarrow O(^1D) + O(^1S)$	$3.90 \times 10^{-10}\tau_e^{-0.7}$	
	$[T_e < 1,200]$	
	$3.86 \times 10^{-10}\tau_e^{-0.61}$	
	$[T_e \geq 1,200]$	
$N^+ + O_2 \rightarrow O_2^+ + N$	1.93×10^{-10}	
$N^+ + O_2 \rightarrow O_2^+ + N(^2D)$	8.25×10^{-11}	
$O_2^+ + N(^2D) \rightarrow N^+ + O_2$	2.5×10^{-10}	
$N^+ + O_2 \rightarrow NO^+ + O(^1D)$	1.98×10^{-10}	
$N^+ + O_2 \rightarrow NO^+ + O$	4.95×10^{-11}	
$N^+ + O_2 \rightarrow O^+ + NO$	2.8×10^{-11}	

Table A1
Continued

Reaction	Rate coefficient (cm^3/s)	Reference
$N^+ + NO \rightarrow NO^+ + N$	$5.73 \times 10^{-9}\ T_n^{-0.44}$	
$N^+ + NO \rightarrow N_2^+ + O$	$7.08 \times 10^{-10}\ T_n^{-0.44}$	
$N^+ + O \rightarrow O^+ + N$	2.2×10^{-12}	
$NO^+ + e \rightarrow O + N(^2D)$	$2.66 \times 10^{-7} \tau_e^{-0.69}$	
	$[T_e < 1,200]$	
	$2.30 \times 10^{-7} \tau_e^{-0.56}$	
	$[T_e \geq 1,200]$	
$NO^+ + e \rightarrow O + N$	$8.40 \times 10^{-8} \tau_e^{-0.69}$	
	$[T_e < 1,200]$	
	$7.25 \times 10^{-8} \tau_e^{-0.56}$	
	$[T_e \geq 1,200]$	
$N + O_2 \rightarrow NO + O$	$1.5 \times 10^{-11} e^{\frac{-3,600}{T_n}}$	Barth et al. (2009)
$N + O \rightarrow NO$	$3.33 \times 10^{-16}\ T_n^{-0.5}$	
	$\times(1 - 0.567\ T_n^{-0.5})$	
$N(^2D) + O_2 \rightarrow NO + O$	$5.58 \times 10^{-12} \tau_n$	
$N(^2D) + O_2 \rightarrow NO + O(^1D)$	$6.2 \times 10^{-13} \tau_n$	
$N(^2D) + N_2 \rightarrow N + N_2$	$10^{-13} e^{\frac{-510}{T_n}}$	
$N(^2D) + e \rightarrow N + e$	$3.8 \times 10^{-12}\ T_e^{0.81}$	
$N(^2D) + O \rightarrow N + O$	1.26×10^{-12}	
$N(^2D) + O \rightarrow N + O(^1D)$	1.4×10^{-13}	
$N(^2D) + O \rightarrow NO^+ + e$	$2.5 \times 10^{-18}\ T_n^{0.5}$	
	$\times(2,205 + T_n) e^{\frac{-4410}{T_n}}$	
$N(^2D) + O^+ \rightarrow N^+ + O$	1.3×10^{-10}	
$N + NO \rightarrow N_2 + O$	$1.6 \times 10^{-10} e^{\frac{-460}{T_n}}$	Barth et al. (2009)
$N(^2D) + NO \rightarrow N_2 + O$	7×10^{-11}	Barth (1992)
$N(^2D) + NO \rightarrow N + NO$	6.7×10^{-11}	
$O + e \rightarrow O(^1D) + e$	$0.15\ T_e^{0.5} \frac{8,537+T_e}{(34,191+T_e)^3}\ e^{\frac{-22,756}{T_e}}$	Mantas and Carlson (1991)
$O(^1D) + N_2 \rightarrow O + N_2$	$1.8 \times 10^{-11} e^{\frac{107}{T_n}}$	
$O(^1D) + O_2 \rightarrow O + O_2$	$3.2 \times 10^{-11} e^{\frac{67}{T_n}}$	
$O(^1D) + NO \rightarrow O + NO$	1.5×10^{-10}	
$O(^1D) + e \rightarrow O + e$	$8.1 \times 10^{-10} \tau_e^{0.5}$	
$O(^1D) + O \rightarrow O + O$	2.5×10^{-11}	
$O(^1S) + O \rightarrow O + O$	2×10^{-14}	
$O(^1S) + O_2 \rightarrow O + O_2$	$1.6 \times 10^{-12} e^{-\frac{6,750-0.0151T_n^2}{8.314T_n}}$	
$O(^1S) + O_2 \rightarrow O(^1D) + O_2$	$7.2 \times 10^{-13} e^{-\frac{6,750-0.0151T_n^2}{8.314T_n}}$	
$O(^1S) + e \rightarrow O + e$	$1.56 \times 10^{-9} \tau_e^{0.94}$	
$O(^1S) + e \rightarrow O(^1D) + e$	8.56×10^{-9}	
$O(^1S) + NO \rightarrow O(^1D) + NO$	5.12×10^{-11}	
$O(^1S) + NO \rightarrow O + NO$	2.88×10^{-11}	
$N^+ + e \rightarrow N$	$3.6 \times 10^{-12} (\frac{250}{T_e})^{0.7}$	
$O^+ + e \rightarrow O$	$3.7 \times 10^{-12} (\frac{250}{T_e})^{0.7}$	
$N_2(v > 11) + O \rightarrow NO + N$	10^{-11}	Pavlov (2011) p.164
$NO + O \rightarrow NO_2 + h\nu_{cont}$	10^{-20}	Hedin et al. (2012)

Table A1
Continued

Reaction	Rate coefficient (cm^3/s)	Reference
$O(^1D) \rightarrow O + h\nu_{630.0nm}$	$A = 8.59 \times 10^{-3} s^{-1}$	
$O(^1S) \rightarrow O(^1D) + h\nu_{557.7nm}$	$A = 1.26 s^{-1}$	
$O(^1S) \rightarrow O + h\nu_{297.2nm}$	$A = 7.5 \times 10^{-2} s^{-1}$	
$N(^2D) \rightarrow N + h\nu_{520.0nm}$	$A = 6.6 \times 10^{-6} s^{-1}$	

Acknowledgments
The authors acknowledge funding by NASA's Explorers Program under the Ionospheric Connection Explorer (ICON) Contracts NNG12FA45C and NNG12FA42I. Experimental and observational data were neither used nor created for this research. Reaction rate coefficients needed to reproduce the analyses are provided in Appendix A. The photochemical model used in this work was written in Python 3 and is available at https://github.com/bharding512/STEVE_NO2.

References

Aladjev, G. A., & Kirillov, A. S. (1995). Vibrational kinetics of molecular nitrogen and its role in the composition of the polar thermosphere. *Advances in Space Research*, *16*(1), 109–112. https://doi.org/10.1016/0273-1177(95)00106-O

Anderson, P. C., Heelis, R. A., & Hanson, W. B. (1991). The ionospheric signatures of rapid subauroral ion drifts. *Journal of Geophysical Research*, *96*(A4), 5785. https://doi.org/10.1029/90ja02651

Archer, W. E., Gallardo-Lacourt, B., Perry, G., St.-Maurice, J. P., Buchert, S. C., & Donovan, E. (2019). STEVE: The optical signature of intense subauroral ion drifts. *Geophysical Research Letters*, *46*, 6279–6286. https://doi.org/10.1029/2019GL082687

Archer, W. E., St.-Maurice, J., Gallardo-Lacourt, B., Perry, G. W., Cully, C. M., Donovan, E., et al. (2019). The vertical distribution of the optical emissions of a STEVE and picket fence event. *Geophysical Research Letters*, *46*, 10,719–10,725. https://doi.org/10.1029/2019GL084473

Barth, C. A. (1992). Nitric oxide in the lower thermosphere. *Planetary and Space Science*, *40*(2-3), 315–336. https://doi.org/10.1016/0032-0633(92)90067-X

Barth, C. A. (2010). Joule heating and nitric oxide in the thermosphere, 2. *Journal of Geophysical Research*, *115*, A10305. https://doi.org/10.1029/2010JA015565

Barth, C. A., Lu, G., & Roble, R. G. (2009). Joule heating and nitric oxide in the thermosphere. *Journal of Geophysical Research*, *114*, A05301. https://doi.org/10.1029/2008JA013765

Bilitza, D., Altadill, D., Truhlik, V., Shubin, V., Galkin, I., Reinisch, B., & Huang, X. (2017). International Reference Ionosphere 2016: From ionospheric climate to real-time weather predictions. *Space Weather*, *15*, 418–429. https://doi.org/10.1002/2016SW001593

Branscomb, L. M. (1962). Photodetachment. In D. R. Bates (Ed.), *Atomic and molecular processes* (pp. 100–140). New York: Academic Press.

Campbell, L., Cartwright, D. C., & Brunger, M. J. (2007). Role of excited N_2 in the production of nitric oxide. *Journal of Geophysical Research*, *112*, A08303. https://doi.org/10.1029/2007JA012337

Enell, C. F., Hedin, J., Stegman, J., Witt, G., Friedrich, M., Singer, W., et al. (2011). The Hotel Payload 2 campaign: Overview of NO, O and electron density measurements in the upper mesosphere and lower thermosphere. *Journal of Atmospheric and Solar-Terrestrial Physics*, *73*(14-15), 2228–2236. https://doi.org/10.1016/j.jastp.2011.01.001

Foster, J. C., Buonsanto, M. J., Mendillo, M., Nottingham, D., Rich, F. J., & Denig, W. (1994). Coordinated stable auroral red arc observations: Relationship to plasma convection. *Journal of Geophysical Research*, *99*(A6), 11429. https://doi.org/10.1029/93JA03140

Gallardo-Lacourt, B., Nishimura, Y., Donovan, E., Gillies, D. M., Perry, G. W., Archer, W. E., et al. (2018). A statistical analysis of STEVE. *Journal of Geophysical Research: Space Physics*, *123*, 9893–9905. https://doi.org/10.1029/2018JA025368

Gillies, D. M., Donovan, E., Hampton, D., Liang, J., Connors, M., Nishimura, Y., et al. (2019). First observations from the TREx spectrograph: The optical spectrum of STEVE and the picket fence phenomena. *Geophysical Research Letters*, *46*, 7207–7213. https://doi.org/10.1029/2019GL083272

Grubbs, G., Michell, R., Samara, M., Hampton, D., Hecht, J., Solomon, S., & Jahn, J. M. (2018). A comparative study of spectral auroral intensity predictions from multiple electron transport models. *Journal of Geophysical Research: Space Physics*, *123*, 993–1005. https://doi.org/10.1002/2017JA025026

Hedin, J., Rapp, M., Khaplanov, M., Stegman, J., & Witt, G. (2012). Observations of NO in the upper mesosphere and lower thermosphere during ECOMA 2010. *Annales Geophysicae*, *30*(11), 1611–1621. https://doi.org/10.5194/angeo-30-1611-2012

Heelis, R. (2004). Electrodynamics in the low and middle latitude ionosphere: A tutorial. *Journal of Atmospheric and Solar-Terrestrial Physics*, *66*(10), 825–838. https://doi.org/10.1016/j.jastp.2004.01.034

Kaufman, F. (1973). The air afterglow revisited, *Chemiluminescence and bioluminescence* (pp. 83–100). Boston, MA: Springer US. https://doi.org/10.1007/978-1-4757-0638-3_7

Khalipov, V. L., Galperin, Y. I., Stepanov, A. E., & Shestakova, L. V. (2001). Formation of a polarization jet during the expansion phase of a substorm: Results of ground-based measurements. *Cosmic Research*, *39*(3), 226–235. https://doi.org/10.1023/A:1017573319665

Khalipov, V. L., Stepanov, A. E., Ievenko, I. B., Kotova, G. A., & Panchenko, V. A. (2018). Formation of red arc in the polarization jet band. *Journal of Atmospheric and Solar-Terrestrial Physics*, *179*, 494–503. https://doi.org/10.1016/j.jastp.2018.08.005

Kozyra, J. U., Nagy, A. F., & Slater, D. W. (1997). High-altitude energy source(s) for stable auroral red arcs. *Reviews of Geophysics*, *35*(2), 155. https://doi.org/10.1029/96RG03194

Liang, J., Donovan, E., Connors, M., Gillies, D., St-Maurice, J. P., Jackel, B., et al. (2019). Optical spectra and emission altitudes of double layer STEVE: A case study. *Geophysical Research Letters*, *46*, 13,630–13,639. https://doi.org/10.1029/2019GL085639

MacDonald, E. A., Donovan, E., Nishimura, Y., Case, N. A., Megan Gillies, D., Gallardo-Lacourt, B., et al. (2018). New science in plain sight: Citizen scientists lead to the discovery of optical structure in the upper atmosphere. *Science Advances*, *4*(3), 16–21. https://doi.org/10.1126/sciadv.aaq0030

Mantas, G. P., & Carlson, H. C. (1991). Reexamination of the O(3 P- 1 D) excitation rate by thermal electron impact. *Geophysical Research Letters*, *18*(2), 159–162. https://doi.org/10.1029/91GL00019

Mcdade, I. C., Llewellyn, E. J., Greer, R. G., & Murtagh, D. P. (1986). ETON 3: Altitude profiles of the nightglow continuum at green and near infrared wavelengths. *Planetary and Space Science*, *34*(9), 801–810. https://doi.org/10.1016/0032-0633(86)90076-0

Mende, S. B., Harding, B. J., & Turner, C. (2019). Subauroral Green STEVE arcs: Evidence for low-energy excitation. *Geophysical Research Letters*, *46*, 14,256–14,262. https://doi.org/10.1029/2019GL086145

Mende, S. B., Swenson, G. R., & Llewellyn, E. J. (1988). Ram glow: Interaction of space vehicles with the natural atmosphere. *Advances in Space Research*, *8*(1), 229–241. https://doi.org/10.1016/0273-1177(88)90368-7

Mendillo, M., Baumgardner, J., & Wroten, J. (2016). SAR arcs we have seen: Evidence for variability in stable auroral red arcs. *Journal of Geophysical Research: Space Physics*, *121*, 245–262. https://doi.org/10.1002/2015JA021722

Mishin, E., & Telegin, V. (1989). The effect of plasma turbulence in aurorae. *Geomagnetism and Aeronomy*, *29*, 1–14.

Nishimura, Y., Gallardo-Lacourt, B., Zou, Y., Mishin, E., Knudsen, D. J., Donovan, E. F., et al. (2019). Magnetospheric signatures of STEVE: Implications for the magnetospheric energy source and interhemispheric conjugacy. *Geophysical Research Letters*, *46*, 5637–5644. https://doi.org/10.1029/2019GL082460

Pavlov, A. V. (2011). Vibrationally excited N_2 and O_2 in the upper atmosphere: A review. *Geomagnetism and Aeronomy*, *51*(2), 143–169. https://doi.org/10.1134/S0016793211020149

Pavlov, A. V. (2014). Photochemistry of ions at *D*-region altitudes of the ionosphere: A review. *Surveys in Geophysics*, *35*(2), 259–334. https://doi.org/10.1007/s10712-013-9253-z

Picone, J. M., Hedin, A. E., Drob, D. P., & Aikin, A. C. (2002). NRLMSISE-00 empirical model of the atmosphere: Statistical comparisons and scientific issues. *Journal of Geophysical Research*, *107*(A12), 1–16. https://doi.org/10.1029/2002JA009430

Richards, P. G., Nicolls, M. J., St.-Maurice, J. P., Goodwin, L., & Ruohoniemi, J. M. (2014). Investigation of sudden electron density depletions observed in the dusk sector by the Poker Flat, Alaska incoherent scatter radar in summer. *Journal of Geophysical Research: Space Physics*, *119*, 10,608–10,620. https://doi.org/10.1002/2014JA020541

Rodger, A. S., Moffett, R. J., & Quegan, S. (1992). The role of ion drift in the formation of ionisation troughs in the mid- and high-latitude ionosphere—A review. *Journal of Atmospheric and Terrestrial Physics*, *54*(1), 1–30. https://doi.org/10.1016/0021-9169(92)90082-V

Sazykin, S., Fejer, B. G., Galperin, Y. I., Zinin, L. V., Grigoriev, S. A., & Mendillo, M. (2002). Polarization jet events and excitation of weak SAR arcs. *Geophysical Research Letters*, *29*(12), 1586. https://doi.org/10.1029/2001GL014388

Sheehan, C. H., & St.-Maurice, J. P. (2004). Dissociative recombination of N_2^+, O_2^+, and NO^+: Rate coefficients for ground state and vibrationally excited ions. *Journal of Geophysical Research*, *109*, A03302. https://doi.org/10.1029/2003JA010132

Sheese, P. E., Gattinger, R. L., Llewellyn, E. J., Boone, C. D., & Strong, K. (2011). Nighttime nitric oxide densities in the Southern Hemisphere mesosphere-lower thermosphere. *Geophysical Research Letters*, *38*, L15812. https://doi.org/10.1029/2011GL048054

Solomon, S., Barth, C. A., & Bailey, S. M. (1999). Auroral production of nitric oxide measured by the SNOE satellite. *Geophysical Research Letters*, *26*(9), 1259–1262. https://doi.org/10.1029/1999GL900235

Solomon, S., Hays, P. B., & Abreu, V. (1988). The auroral 6300 Å emission: Observations and modeling. *Journal of Geophysical Research*, *93*(A9), 9867. https://doi.org/10.1029/JA093iA09p09867

St.-Maurice, J. P., & Laneville, P. J. (1998). Reaction rate of O^+ with O_2, N_2, and NO under highly disturbed auroral conditions. *Journal of Geophysical Research*, *103*(A8), 17,519–17,521. https://doi.org/10.1029/98JA01387

Stevens, M. H., Conway, R. R., Cardon, J. G., & Russell, J. M. (1997). MAHRSI observations of nitric oxide in the mesosphere and lower thermosphere. *Geophysical Research Letters*, *24*(24), 3213–3216. https://doi.org/10.1029/97GL03257

Zipf, E. C., Borst, W. L., & Donahue, T. M. (1970). A mass spectrometer observation of NO in an auroral arc. *Journal of Geophysical Research*, *75*(31), 6371–6376. https://doi.org/10.1029/ja075i031p06371